

Enhanced Yield Rate of ^{229m}Th via Cascade Decay in Storage Rings and Electron Beam Ion Traps

Yumiao Wang , Yi Yang , Yixin Li , Ding Yue , Kai Zhao , Youjing Wang , Changbo Fu , ^{*} and Yugang Ma 

Key Laboratory of Nuclear Physics and Ion-beam Application (MoE),
Institute of Modern Physics, Fudan University, Shanghai 200433, China

(Dated: February 2, 2026)

The low-energy nuclear isomeric state of ^{229m}Th provides a unique bridge between nuclear and atomic physics, enabling applications such as nuclear clocks and precision metrology. However, efficient and controllable production of ^{229m}Th remains a major experimental challenge. We propose an efficient scheme to produce the ^{229m}Th in storage rings (SRs) and electron beam ion traps (EBITs), using a cascade decay pathway. Highly charged ions are excited to higher nuclear states via nuclear excitation by inelastic electron scattering (NEIES) and nuclear excitation by electron capture (NEEC), followed by radiative or internal conversion cascades that populate the isomer. Our calculations demonstrate that, under typical SRs and EBITs conditions, optimized indirect excitation pathways significantly enhance ^{229m}Th production rate. In particular, NEIES can provide an enhancement of up to four orders of magnitude through cascade de-excitation at high energies, while NEEC can contribute an additional enhancement of up to several tens of times. Such a significant increase in the ^{229m}Th yield rate would facilitate its application in various nuclear photonics fields, especially in the development of atomic nuclear clocks.

I. INTRODUCTION

The low-lying isomeric state of ^{229m}Th at 8.36 eV [1, 2] has attracted intense interest due to its potential applications in nuclear optical clocks [3–7], nuclear lasers [8], tests of fundamental constants [9, 10], searching for dark matter [11], and nuclear-based frequency standards [12].

Despite this remarkable progress in spectroscopic characterization [12–19], the efficient and controllable production of ^{229m}Th remains one of the key challenges for both crystal-based [12–14, 20–22] and ion-trap-based [23–27] applications. ^{229m}Th can be produced through the α decay of ^{233}U [23, 28–32] or the β decay of ^{229}Ac [33, 34], but with very limited production rates. Direct laser excitation in Th-doped crystals has been demonstrated [12–14], but the excitation efficiency remains extremely low, and high-power continuous-wave VUV sources are still under development [35–37]. Alternative indirect schemes via higher-lying nuclear states, including the second excited state at 29.19 keV, have been explored using synchrotron radiation [38], yet they require large-scale facilities and offer limited tunability.

To produce ^{229m}Th with an efficient mechanism, electron-mediated nuclear excitation may provide a versatile and controllable alternative, with two mechanisms being particularly relevant: nuclear excitation by inelastic electron scattering (NEIES, also known as Coulomb excitation, CE) [39–43] and nuclear excitation by electron capture (NEEC, or inverse internal conversion, IIC) [41, 44–52]. In NEIES, free electrons transfer part of their kinetic energy to the nucleus through inelastic collisions whenever the electron energy exceeds the excitation threshold. NEEC, in contrast, is a resonant process in which a free electron is captured into a bound electronic state of an ion while simultaneously exciting the nucleus, enabling selective and efficient population of nuclear states. The ^{229}Th isomer has been studied theoretically under the NEIES and NEEC mechanisms [43, 49, 52], focusing on its first and second excited states. Experimentally,

electron-mediated excitations of ^{229}Th have not yet been realized [40, 43, 53, 54]. In addition, the NEEC process has not yet been confirmed [46, 55–58]. Both processes are significantly enhanced in highly charged ions (HCIs) [44, 59, 60], where reduced electronic shielding strengthens the electron-nucleus coupling, making HCIs ideal for exploiting controlled excitation pathways.

There are two experimental platforms for producing HCIs, storage rings (SRs) [50, 62–64] and electron beam ion traps (EBITs) [48, 60, 65, 66], which are suitable for ^{229m}Th producing applications [49]. In SRs, circulating HCIs interact with an electron cooler or a dedicated electron target, enabling nuclear excitation and downstream detection of isomers. In EBITs, HCIs are produced and confined by a compressed, tunable electron beam combined with magnetic and electrostatic fields. In these apparatuses, the NEIES and NEEC processes dominate the production of ^{229m}Th [49, 67], making them critical to the design of electron-driven isomeric excitation schemes. NEIES occurs whenever the electron energy exceeds the excitation threshold, while NEEC can be resonantly induced.

The selected excitation scheme to higher levels, followed by cascade decay to the ^{229}Th isomeric state, is shown in Fig. 1. As discussed by Chen et al. [68], by using the projected shell model, some nuclear transition probabilities of higher-lying states of ^{229}Th are relatively large. Therefore, the cascade decay to the isomeric state can be utilized to optimize isomer yield, and then may achieve significantly higher efficiency compared to direct excitation methods.

In this work, we present a theoretical investigation of electron-mediated excitation pathways leading to ^{229m}Th via cascade decay under SR and EBIT conditions. We calculate NEIES and NEEC cross sections, excitation rates, and their dependence on electron energy, charge state, and electronic configuration, providing quantitative guidance for optimizing isomer production and informing the design of future nuclear-clock and NEEC experiments.

The remainder of this paper is organized as follows. Section II introduces the theoretical framework for NEIES and NEEC, as well as the procedures used to compute electronic wave functions. Section III presents energy-dependent cross

* cbfu@fudan.edu.cn

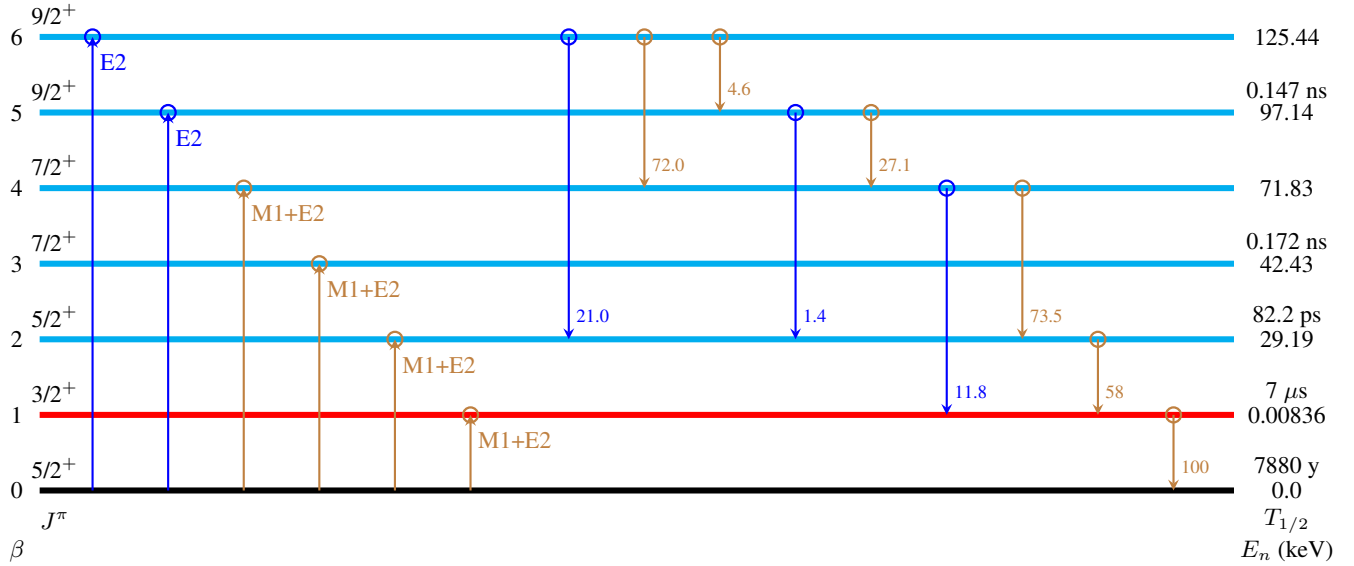


FIG. 1. Partial level scheme of ^{229}Th showing selected nuclear excited states and their decay pathways to the isomeric state. The M1+E2 and E2 transitions in the decay paths are marked in brown and blue, respectively. For each nuclear level β , the spin-parity assignment J^π , half-life $T_{1/2}$, and excitation energy E_n are labeled on either side of the corresponding level line. The upper-right label on each arrow indicates the branching ratio of the corresponding decay channel (in %). The energy and lifetime of the first excited state are taken from [8], and those of the second excited state are also taken from [38]. For the branching ratios of different decay channels, the values for the second excited state are taken from [38], while the others are calculated using the formulas Eqs. (10), with the relevant data obtained from [61]. Unless otherwise specified, all other data are also taken from [61].

sections and production rates for different pathways under EBIT and SR conditions. The main results and an outlook for experimental implementations will be presented at the end.

II. THEORETICAL FRAMEWORK OF ELECTRONIC PROCESSES

In the SR and EBIT environments, the isomeric producing mechanisms are the NEIES and NEEC, which are briefly introduced in the following sections. Throughout this paper, atomic units (a.u.) are employed, such that $\hbar = m_e = e = 1$ and $c = 1/\alpha$. In these units, \hbar represents the reduced Planck constant, m_e the mass of the electron, e the elementary charge, c the speed of light, and α the fine-structure constant.

A. NEIES cross section

The detailed calculations of NEIES and NEEC have been extensively discussed in previous works [41]. Therefore, we present only the final expression for the NEIES cross section,

which is expressed as

$$\begin{aligned} \sigma_{\text{NEIES}}(E_i) = & \frac{8\pi^2}{c^4} \frac{E_i + c^2}{p_i^3} \frac{E_f + c^2}{p_f} \\ & \times \sum_{T,\lambda} \frac{k^{2\lambda+2}}{(2\lambda-1)!!^2} B(T\lambda, J_i \rightarrow J_f) \\ & \times \sum_{l_i, j_i, l_f, j_f} \frac{(2l_i+1)(2l_f+1)(2j_i+1)(2j_f+1)}{(2\lambda+1)^2} \\ & \times \begin{pmatrix} l_f & l_i & \lambda \\ 0 & 0 & 0 \end{pmatrix}^2 \left\{ \begin{matrix} l_i & \lambda & l_f \\ j_f & 1/2 & j_i \end{matrix} \right\}^2 |R_{fi}^{T\lambda}|^2. \end{aligned} \quad (1)$$

Here, the subscripts i and f label the initial and final electronic states, while the indices n and e distinguish nuclear and electronic quantities. In Eq. (1), E_i and E_f denote the energies of the incident and outgoing electrons, with corresponding momenta p_i and p_f . The factor $k = E_n/c$ represents the nuclear excitation energy divided by the speed of light, while T and λ specify the type (electric or magnetic) and multipolarity of the nuclear transition. $B(T\lambda, J_i \rightarrow J_f)$ is the reduced nuclear transition probability characterizing the intrinsic strength of the nuclear transition between initial and final nuclear states with spins J_i and J_f . The sums over l_i , j_i , l_f , and j_f account for the possible angular momentum couplings of the electronic states, with n , l , j , and m denoting the principal quantum number, orbital angular momentum, total angular momentum, and magnetic quantum number of the initial and final electronic states, respectively.

The radial transition matrix element $R_{fi}^{T\lambda}$ measures the overlap between the initial and final electronic Dirac wave-

functions, representing the electronic contribution to the interaction between the electron and the nucleus. The same formalism is, in principle, also applicable to the NEEC process. For electric transitions, one has

$$R_{fi}^{E\lambda} = \int_0^\infty h_\lambda^{(1)}(kr) [g_i(r)g_f(r) + f_i(r)f_f(r)] r^2 dr, \quad (2)$$

and for magnetic transitions,

$$R_{fi}^{M\lambda} = \frac{\kappa_i + \kappa_f}{\lambda} \times \int_0^\infty h_\lambda^{(1)}(kr) [g_i(r)f_f(r) + g_f(r)f_i(r)] r^2 dr. \quad (3)$$

Here, $\kappa = (l - j)(2j + 1)$ is conventionally used as shorthand notation for j and l , and $h_\lambda^{(1)}(kr)$ represents the spherical Hankel function of the first kind.

The radial components of the electronic wave functions, $g(r)$ and $f(r)$, correspond to the initial and final states, respectively. In this work, both bound and continuum Dirac wave functions are computed using the RADIAL package [69]. The underlying electron potential is obtained within the Dirac-Hartree-Fock-Slater framework [70, 71], which incorporates the nuclear, direct electronic, and exchange contributions in a self-consistent manner. The detailed formulation of the DHFS potential can be found in Refs. [43, 52].

B. NEEC cross section

The NEEC cross section [41] can be given by

$$\begin{aligned} \sigma_{\text{NEEC}}(E_i) = & \frac{8\pi^3}{c^2} \frac{E_i + c^2}{p_i^3} \\ & \times \sum_{T,\lambda} \frac{k^{2\lambda+2}}{(2\lambda - 1)!!^2} B(T\lambda, J_i \rightarrow J_f) \\ & \times \sum_{l_i, j_i, l_f, j_f} \frac{(2l_i + 1)(2l_f + 1)(2j_i + 1)(2j_f + 1)}{(2\lambda + 1)^2} \\ & \times \begin{pmatrix} l_f & l_i & \lambda \\ 0 & 0 & 0 \end{pmatrix}^2 \begin{Bmatrix} l_i & \lambda & l_f \\ j_f & 1/2 & j_i \end{Bmatrix}^2 |R_{fi}^{T\lambda}|^2 \\ & \times L_{\text{NEEC}}(E_i - E_r). \end{aligned} \quad (4)$$

Here, E_r represents the resonance energy of the recombining electron. The function L_{NEEC} represents the normalized Lorentz profile occurring in resonant systems,

$$L_{\text{NEEC}}(E_i - E_r) = \frac{\Gamma_{\text{NEEC}}/2\pi}{(E_i - E_r)^2 + \Gamma_{\text{NEEC}}^2/4}. \quad (5)$$

In the above expression, the natural width of the resonant state, Γ_{NEEC} , consists of two main contributions: the width of the final electronic state, Γ_f , associated with spontaneous photon emission, and the nuclear decay width, $\Gamma_n = \Gamma_\gamma + \Gamma_{\text{IC}}$, which includes both the γ -decay width, Γ_γ , and the internal conversion width, Γ_{IC} . When the electron is captured directly into the ionic ground state, the total width reduces to

$\Gamma_{\text{NEEC}} = \Gamma_n$. In contrast, if the capture occurs into an excited electronic state, the total width becomes $\Gamma_{\text{NEEC}} = \Gamma_n + \Gamma_f$.

In cases where the incident electron energy is distributed rather than sharply defined, an integration over the electron energy becomes necessary. To simplify the treatment of this effect, the concept of resonant strength is employed as

$$S_{\text{NEEC}} = \int dE_i \sigma_{\text{NEEC}}(E_i). \quad (6)$$

C. Excitation rate

For a given excitation channel $0 \rightarrow \beta$, the NEIES and NEEC excitation rates per target particle are obtained by convoluting the corresponding electric and magnetic transition cross sections with the electron flux energy distribution $\Phi_e(E_i)$ over the incident electron energy E_i . They are calculated by

$$\lambda_{\text{NEIES/NEEC}} = \int dE_i \sigma_{\text{NEIES/NEEC}}(E_i) \Phi_e(E_i). \quad (7)$$

Owing to the extremely narrow width of the NEEC resonance relative to the energy spread of the incident electron, the process can be treated within the resonance approximation, where the energy dependence of the cross section is represented by a Dirac delta function, $\delta(E_i - E_r)$. Specifically, in the case of NEEC, the excitation rate can be equivalently expressed in terms of the resonance strength S as $\lambda_{\text{NEEC}} = S_{\text{NEEC}} \Phi_e(E_r)$.

Based on the electron beam parameters, the electron flux $\Phi_e(E_i)$ is modeled as a Gaussian distribution

$$\Phi_e(E_i) = \frac{I_e}{eA_e \epsilon_e \sqrt{\pi}} \exp \left[- \left(\frac{E_i - E_{ir}}{\epsilon_e} \right)^2 \right]. \quad (8)$$

Here, E_{ir} is a function of central electron energy, $I_e = en_e v_e$ is the electron beam current, e is the elementary charge (1.602×10^{-19} C), ϵ_e is the electron beam energy spread, and A_e is the beam cross-sectional area, determined from a radius of r_e .

For the non-resonant NEIES process, the cross section exhibits only a weak energy dependence within the narrow energy window ϵ_e defined by the electron energy distribution, and can thus be reasonably approximated as a constant, $\sigma_{\text{NEIES}}(E_i) \approx \sigma_0$, over the relevant energy range. Under this approximation, the convolution integral reduces to the standard Gaussian normalization. Thus, λ_{NEIES} simplifies to $\lambda_{\text{NEIES}} = I_e/(e A_e) \sigma_0$.

In general, the characteristic timescales of the nuclear excitation processes are much shorter than the decay lifetime of the isomeric state: the de-excitation of higher-lying excited states to the isomer occurs on the order of nanoseconds, whereas the isomer itself decays to the ground state on the microsecond timescale. Therefore, unlike Ref. [43], we do not employ a dynamical model that simultaneously describes excitation and decay, and instead neglect the temporal evolution of the isomer population in ^{229}Th .

In order to calculate the population rate of the first excited nuclear state, it is necessary to determine the branching ratios (BRs) of higher-lying states decaying into it. The BR of the second excited state is directly taken from the experimental results reported in Ref. [38], while those of other states are obtained from experimental data compiled in the NNDC database [61]. The corresponding formulas used for the calculations are presented below.

Consider an excited state that decays via multiple γ transitions or IC, with no other particle decay channels. Let $I_{\beta \rightarrow \beta'}$ represent the measured γ -ray intensity of the $\beta \rightarrow \beta'$ transition, and let $\alpha_{\beta \rightarrow \beta'}^{\text{eff}}$ denote the associated effective internal conversion coefficient (ICC), where $0 \leq \beta' < \beta$. For a transition with mixed multipolarity (e.g., M1+E2), the effective ICC is

$$\alpha_{\beta \rightarrow \beta'}^{\text{eff}} = \frac{\alpha_{M,\beta \rightarrow \beta'} + \delta_{\beta \rightarrow \beta'}^2 \alpha_{E,\beta \rightarrow \beta'}}{1 + \delta_{\beta \rightarrow \beta'}^2}, \quad (9)$$

where $\delta_{\beta \rightarrow \beta'}$ denotes the mixing ratio, reflecting the relative strength of the electric and magnetic components, and $\alpha_{T,\beta \rightarrow \beta'}$ is the corresponding ICC. The BR of each decay channel to the isomeric state is defined as the fraction of the total decay strength

$$\text{BR}_{\beta \rightarrow \beta'} = \frac{I_{\beta \rightarrow \beta'} (1 + \alpha_{\beta \rightarrow \beta'}^{\text{eff}})}{\sum_{\beta \rightarrow \beta'} I_{\beta \rightarrow \beta'} (1 + \alpha_{\beta \rightarrow \beta'}^{\text{eff}})}. \quad (10)$$

The effective excitation rate $\lambda_{\text{NEIES/NEEC}}^{\text{eff}}$ is determined by taking into account all possible cascade decay paths from $0 \rightarrow \beta \Rightarrow 1$. Here, the symbol $a \Rightarrow b$ denotes a multi-step cascade process from nuclear state a to state b , for instance, as illustrated in Fig. 1. For a given incident electron energy, the effective excitation rate can be expressed as a sum over all possible cascade paths from state 0 to state 1 via intermediate states β , weighted by the product of the corresponding branching ratios

$$\lambda_{\text{NEIES/NEEC}}^{\text{eff}} = \sum_{0 \rightarrow \beta} \prod_{\beta \Rightarrow 1} \text{BR}_{\beta \Rightarrow 1} \lambda_{\text{NEIES/NEEC}}. \quad (11)$$

Here, the range of β values included depends on whether the corresponding electron energies exceed the energy of the respective nuclear excited state.

In the following section, the ^{229}Th isomer yield rate R_{iso} is described by different expressions under different experimental setups. We first define an enhancement factor $P = R_{\text{iso}}^{0 \rightarrow \beta \Rightarrow 1} / R_{\text{iso}}^{0 \rightarrow 1}$, which represents the relative yield rate of indirect excitation via higher-lying excited states $0 \rightarrow \beta \Rightarrow 1$ compared to direct excitation $0 \rightarrow 1$.

III. OPTIMIZATION RESULTS OF ^{229m}TH PRODUCTION

In the following, the calculated cross sections and corresponding production rates for the SR and EBIT are presented separately, followed by a detailed analysis and discussion.

A. Cross sections calculation

To evaluate the NEIES cross section in Eq. (1) and the NEEC resonance strength in Eq. (6), reduced transition probabilities $B(T\lambda, J_i \rightarrow J_f)$ are required. The values adopted in the present calculations are summarized in Table I, where the $B(T\lambda, J_i \rightarrow J_f)$ for levels 1–5 are taken from the most recent theoretical calculations reported in Ref. [68]. For the sixth excited state, the $B(T\lambda, J_i \rightarrow J_f)$ value is evaluated using the TROPIC program [72], based on the experimental lifetime, γ -ray intensity, and ICC from the NNDC database [61]. Due to the lack of experimental $B(T\lambda, I_i \rightarrow I_f)$ values, theoretical predictions may vary, causing uncertainties in the cross sections [73].

For a given incident electron energy, the NEIES cross section exhibits relatively small sensitivity to the ionic charge state, varying by approximately one order of magnitude at the same energy [42, 43]. In this work, we mainly focus on the NEIES cross section for the highest initial ionic charge state $q_i = 90$, i.e. $^{229}\text{Th}^{90+}$, which generally corresponds to the largest cross-section values among different excitation channels for a given ionic charge state and electron energy, as illustrated in Fig. 2. It is apparent that the cross sections exhibit significant energy-dependent characteristics: in the low-energy region (below around 200 keV), the cross section rapidly reaches its peak near the threshold energy E_n and then decreases with increasing electron energy. Upon entering the high-energy region, the cross sections increase again and span several orders of magnitude; in some cases, the cross section for the fourth excited state even exceeds that of the first excited state, despite being smaller at lower energies. In addition, the cross sections for the fifth and sixth excited states exhibit a pronounced absolute advantage, with values far exceeding those for the direct excitation of the first excited state.

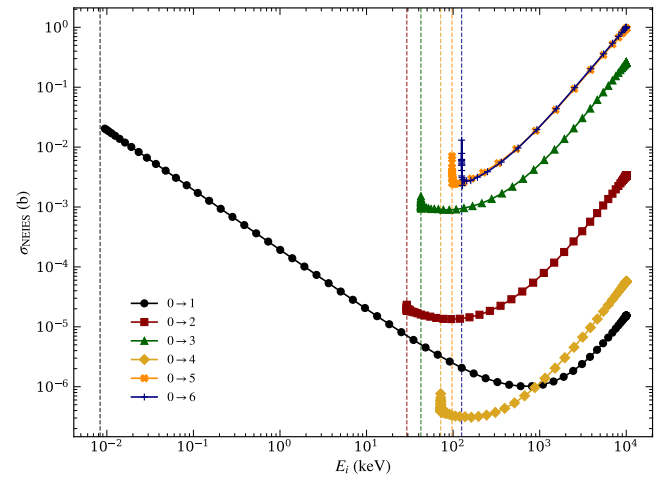


FIG. 2. NEIES cross sections σ_{NEIES} as functions of the incident electron energy E_i for different reaction channels at an ionic charge state of $q_i = 90$. The vertical dashed lines mark the threshold energies corresponding to different excitation channels $0 \rightarrow \beta$.

Regarding the NEEC process, the cross-sections exhibit resonant structures. In this work, the first excited isomer is discussed separately from higher states due to its much lower

TABLE I. Different nuclear transition channels of ^{229}Th , together with the reduced transition probabilities for decays to the ground state (in W.u.). The data in the first five rows are taken from Ref. [68].

$\beta \rightarrow 0$	Level (keV)	J_i^π	J_f^π	$T\lambda$	$B(T\lambda, J_i \rightarrow J_f)$ (W.u.)
1 \rightarrow 0	0.00836	$5/2^+$	$3/2^+$	$M1/E2$	0.0240 / 8.74
2 \rightarrow 0	29.19	$5/2^+$	$5/2^+$	$M1/E2$	0.00339 / 8.4
3 \rightarrow 0	42.43	$5/2^+$	$7/2^+$	$M1/E2$	0.005 / 233.0
4 \rightarrow 0	71.83	$5/2^+$	$7/2^+$	$M1/E2$	0.001 / 0.018
5 \rightarrow 0	97.14	$5/2^+$	$9/2^+$	$E2$	66.4
6 \rightarrow 0	125.44	$5/2^+$	$9/2^+$	$E2$	41.936

excitation energy, on the order of eV, compared with the keV range of the higher states. This difference results in variations in the cross-section distributions. For the first excited isomer at 8.36 eV, only the first few low-charge states satisfy the resonance condition when considering $n < 10$, as shown in Fig. 3. If higher- n Rydberg states, typically with $n \gtrsim 100$, are included [52], high-charge states can also contribute. Under ideal conditions, the maximum NEEC resonance strength S_{NEEC} reaches approximately 0.1 b-eV near the resonance electron energy $E_r \simeq 0.1$ eV. In practice, however, such high- n states may be difficult to realize experimentally with sufficient precision.

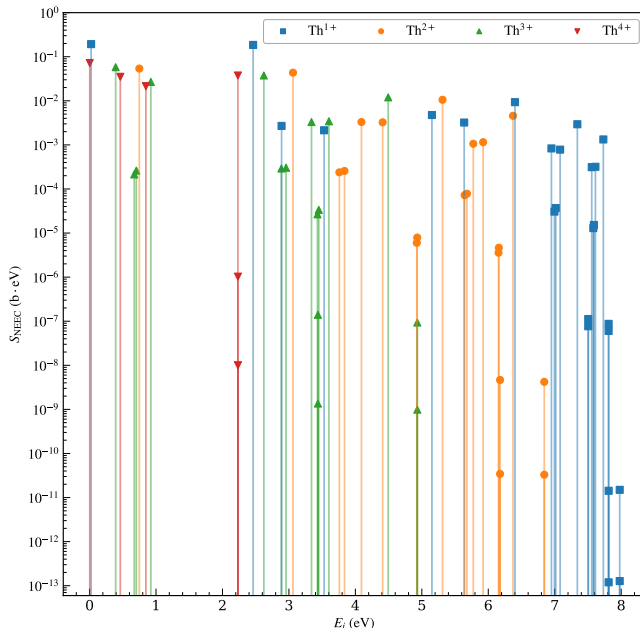


FIG. 3. NEEC resonance strength S_{NEEC} for the $0 \rightarrow 1$ excitation channel at $q_i = 1-4$ when considering $n < 10$.

For the second excited state and higher nuclear states, under the ground-state assumption [47], the highest charge state satisfying the NEEC resonance condition generally corresponds to the global maximum of the cross section among all charge states [49, 52]. Even if this does not coincide with the absolute peak, it typically remains among the largest values. Accordingly, we focus on the case expected to yield the maximum NEEC resonance strength. The ionic charge state $q_i = 90$

is taken as an example for each excitation channel, with the results shown in Fig. 4. The largest S_{NEEC} values are concentrated in the third, fifth, and sixth excited states, reaching roughly 10 b-eV. This is nearly two orders of magnitude higher than that of direct excitation. Therefore, for NEEC excitation, indirect cascade excitation of ^{229}Th appears to be a more suitable approach.

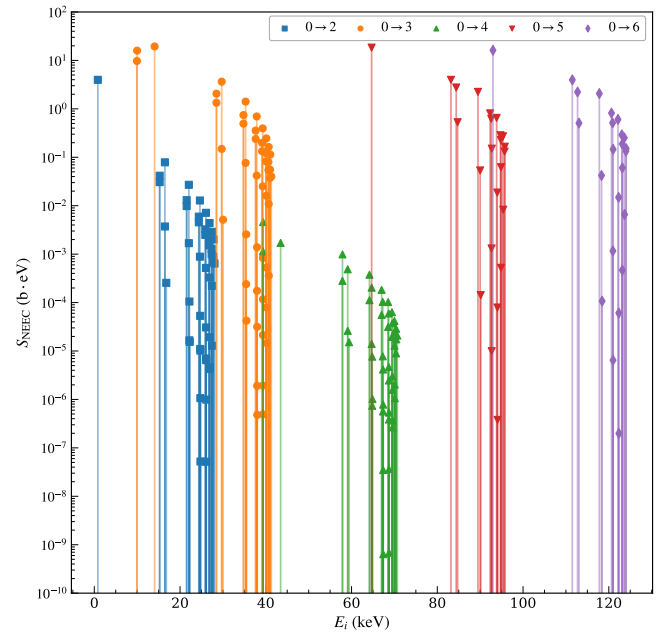


FIG. 4. NEEC resonance strength S_{NEEC} for the $0 \rightarrow 2-6$ excitation channels at a selected representative ionic charge state $q_i = 90$.

B. Yield rates in SRs

In the SR environment, due to the presence of a single ionic charge state, for an electron beam at a given energy, the occurrence of NEIES precludes NEEC, and vice versa. Consequently, the total isomer production rate for all allowed cascade channels, defined as the number of ^{229}Th isomers per unit time, can be expressed as

$$R_{\text{iso}} = R_{\text{NEEC}} + R_{\text{NEIES}} = [\lambda_{\text{NEEC}}^{\text{eff}}(E_i) + \lambda_{\text{NEIES}}^{\text{eff}}(E_i)] \times N_i. \quad (12)$$

Here, $N_i = n_i \pi r_i^2 L_i$ denotes the total number of target ions, where n_i is the target ion density, and r_i and L_i define the radius and length of the ideal cylindrical interaction region, respectively. For a typical SR [43, 49], we assume a total of 10^8 ions in the ring, and an electron beam with a current of $I_e = 200$ mA, a radius of $r_e = 1$ cm, and an energy spread on the order of 1 meV.

For the contribution due to the NEIES mechanism, the calculated isomer production rates are shown in Fig. 5. As the electron energy increases, more excitation channels become accessible, leading to stepwise rises in the total yield rates at low energies. Within the energy range considered here, the total yield rates follow a trend similar to, but slightly higher than, that of the sixth excited state. Compared to the direct excitation of the first excited state, the total yield rates at high electron energies are enhanced by at least 4 orders of magnitude. Finally, since the branching ratio of the third excited state is zero, it does not contribute to the total yield rates across the entire energy range.

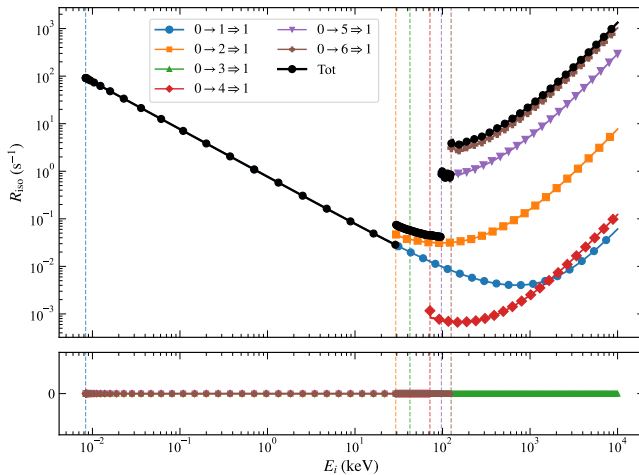


FIG. 5. ^{229m}Th NEIES production rates R_{iso} for different cascade decay channels as shown in Fig. 1 and the total yield rate versus electron energy at $q_i = 90$. Vertical dashed lines denote excitation thresholds. A SR configuration with 10^8 ions, $I_e = 200$ mA, $r_e = 1$ cm, and $\epsilon_e = 1$ meV electron energy spread is assumed.

In the case of the NEEC process, the maximum yield rate for each cascade decay channel occurs at the electron beam energy corresponding to the highest NEEC cross section among all charge states and configurations. Table II lists, for each decay channel, the electron energies at which the NEEC cross section reaches its maximum for $q_i = 90$, along with the resulting isomer population rates for different levels β . Contributions from NEEC and NEIES are shown separately. The cross sections for direct isomer excitation are estimated following Ref. [52], although achieving these would require very high principal quantum numbers n . Notably, the absence of NEEC signals for the third excited state provides a convenient reference for control experiments. The cascade decay channel of the fourth excited state does not lead to an increased yield due to its relatively low cross section. The remaining cascade decay channels exhibit at least an order-of-magnitude enhancement relative to direct excitation, with the sixth excited

state showing the largest increase, reaching approximately a factor of 80.

C. Yield rates in EBITs

In contrast to the SR case, the EBIT offers a plasma environment that supports the production and confinement of HCIs with a distributed charge-state population. If only NEIES is considered, the weak dependence of the NEIES cross sections on the charge state leads to conclusions in an EBIT that are analogous to those in an SR. For schemes incorporating NEEC resonances, a dual-electron-beam configuration [48, 49] is adopted, in which one beam is used for charge breeding, while a second beam with tunable energy is dedicated to resonant NEEC excitation. Accordingly, the ^{229m}Th production rate can be calculated by accounting for the charge-state distribution q_i

$$R_{\text{iso}} = R_{\text{NEEC}} + R_{\text{NEIES}} \\ = \sum_{q_i, E_{ir}, E_{is}} P_{q_i} \left[\lambda_{\text{NEEC}}^{\text{eff}, q_i}(E_i) + \lambda_{\text{NEIES}}^{\text{eff}, q_i}(E_i) \right] \times N_i, \quad (13)$$

where P_{q_i} is the population of ^{229}Th ions in charge state q_i , E_{is} is the electron beam energy used for charge stripping in the dual-electron-gun EBIT device, and E_{ir} is the resonant electron beam energy required for the NEEC process. Assuming an EBIT trapping volume approximated as a perfect cylinder with a radius equal to the electron beam radius, 50 μm , and a length of 3 cm, together with a target ion density of 10^8 cm^{-3} , the total number of target particles is estimated to be $N_i = 2.36 \times 10^4$.

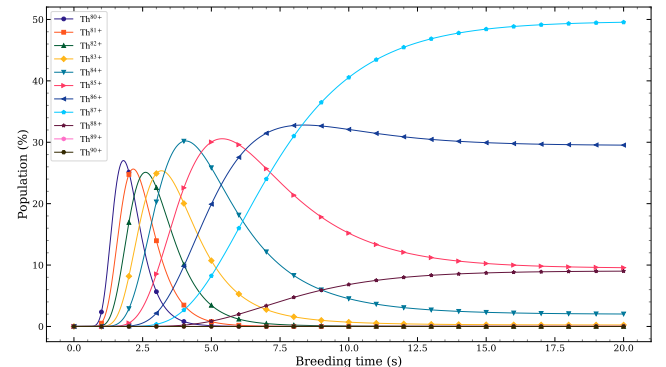


FIG. 6. The charge-breeding process of ^{229}Th ions in an EBIT was simulated using the code `ebitsim`, with the following parameters: electron stripping energy of 130 keV, electron beam current of 200 mA, breeding time of 20 s, and beam radius of 50 μm .

In this work, the time evolution simulation of ionic charge states within the trap is modeled using the charge-breeding simulation package `ebitsim` [74]. The code solves a system of coupled rate equations describing the population dynamics of different ionic charge states under electron-beam irradiation. Building on earlier developments, `ebitsim` allows flexible control of key EBIT parameters, including

TABLE II. 229m Th isomer population rates in a SR for different indirectly excited levels β . R_{iso} denotes the total isomer yield rate, R_{NEEC} the contribution from NEEC, R_{NEIES} the contribution from NEIES, and P the relative yield rate of each indirect excitation scheme compared with direct excitation.

Paths	E_{ir} (keV)	R_{NEEC} (s^{-1})	R_{NEIES} (s^{-1})	R_{iso} (s^{-1})	Dominated by	P
$0 \rightarrow 1$	0.0001	2.24×10^3	0.00	2.24×10^3	NEEC	1.00
$0 \rightarrow 2 \rightarrow 1$	0.822871	5.16×10^4	9.34×10^{-1}	5.16×10^4	NEEC	2.30×10^1
$0 \rightarrow 3 \Rightarrow 1$	14.06784	0.00	5.64×10^{-2}	5.64×10^{-2}	NEIES	2.52×10^{-5}
$0 \rightarrow 4 \Rightarrow 1$	39.37434	5.61×10^1	5.99×10^{-2}	5.62×10^1	NEEC	2.51×10^{-2}
$0 \rightarrow 5 \Rightarrow 1$	64.68429	6.42×10^4	4.61×10^{-2}	6.42×10^4	NEEC	2.87×10^1
$0 \rightarrow 6 \Rightarrow 1$	92.98684	1.89×10^5	4.22×10^{-2}	1.89×10^5	NEEC	8.44×10^1

the electron-beam current and energy, beam diameter, background gas pressure, and the spatial overlap between the electron beam and the trapped ion cloud.

For the charge-breeding simulations of 229 Th ions, the dominant first-order atomic processes are taken into account, namely electron-impact ionization (EI), radiative recombination (RR), and charge exchange (CX) with residual gas atoms. EI drives the population toward higher charge states, whereas RR and CX provide competing loss channels that limit the achievable charge-state distribution. Higher-order processes, such as dielectronic recombination, ion-ion interactions, and nuclear-related processes (e.g., IC), are neglected. This approximation is justified under typical EBIT operating conditions, where the electron density and background gas pressure are sufficiently low. Within this framework, `ebitsim` provides a self-consistent description of the temporal evolution toward charge-state equilibrium and enables systematic exploration of how EBIT operating parameters influence the charge-breeding efficiency and the resulting charge-state distribution of 229 Th ions. For ions in a given charge state q_i , the time evolution of the charge-state population in the trap is governed by

$$\frac{dN_{q_i}}{dt} = EI_{q_i-1} - EI_{q_i} + RR_{q_i+1} - RR_{q_i} + CX_{q_i+1} - CX_{q_i}, \quad (14)$$

which follows the rate-equation approach adopted in Ref. [75]. In this code, ion loss from the trap is neglected due to the deep trapping potential characteristic of EBIT operation.

As shown in Fig. 6, the case with a charge-stripping electron energy of 130 keV, a 200 mA electron beam, a breeding time of 20 s, a beam radius of 50 μ m, and all other parameters set to their default values was simulated. Subsequently, as the simulation indicates that the maximum charge-state population occurs at $q_i = 87+$, a second electron beam providing the resonant energies E_{ir} corresponding to the maximum NEEC cross sections of each decay channel at $q_i = 87+$ is employed. The results are summarized in Table III. It is found that the third and fourth excited states are more favorable for NEIES dominance, as the maximum NEEC cross sections along these cascade decay paths remain relatively small, while NEIES contributes across the full energy range. Other cascade paths, except for the sixth excited state, are in principle not suitable to distinguish NEEC from NEIES, since the theoretical difference between the two mechanisms is only about one order

of magnitude. Moreover, for the sixth cascade path, under 130 keV stripping electron energy and 94.6615 keV resonance electron energy, it provides the largest advantage compared to direct excitation. Here, NEEC dominates and can produce 229 Th isomeric states at a rate of 13.5 s^{-1} , resulting in a total 229m Th yield rate that is 29 times higher than that from direct excitation. In summary, this cascade decay channel enables not only efficient production of 229m Th but also offers a promising route for the experimental verification of the NEEC process.

IV. CONCLUSIONS

In conclusion, to excite 229m Th efficiently, we propose electron-induced excitation schemes based on two typical experimental platforms, SRs and EBITs. These schemes leverage the large excitation cross sections of HCIs and the high efficiency of subsequent cascade decays, which are expected to significantly enhance the yield rate of the 229m Th isomer. The numerical results show that, under the NEIES mechanism across a continuous range of electron energies, the 229m Th yield rate at electron energies above approximately 200 keV can be significantly enhanced. This enhancement occurs along the cascade decay pathways of the fifth and sixth excited states and can exceed that from direct excitation by up to four orders of magnitude. Furthermore, at the NEEC resonance energy, the yield rate can be further increased by dozens of times.

Once a substantial number of 229m Th ions are produced, they can be extracted and loaded into various ion traps, providing valuable input for the development of nuclear clocks. Alternatively, they can be embedded in crystal environments to study their decay modes. The proposed schemes also highlight the potential of using 229 Th in SR and EBIT facilities to investigate the NEEC process.

ACKNOWLEDGMENTS

This work is supported by the National Key Research and Development Program of China (Grant No. 2023YFA1606900), the National Natural Science Foundation of China (Grant Nos. 12235003 and 12447106), and the China Scholarship Council (Grant No. 202406100161).

TABLE III. ^{229m}Th isomer population rates for an EBIT with electron stripping energy $E_{is} = 130$ keV. E_{ir} denotes the resonance electron energy input corresponding to the maximum NEEC cross section for each decay channel. Separate contributions from NEEC and NEIES are listed. R_{iso} denotes the total isomer yield rate, R_{NEEC} the contribution from NEEC, R_{NEIES} the contribution from NEIES, and P the relative yield rate of each indirect excitation scheme compared with direct excitation.

Paths	E_{is} (keV)	E_{ir} (keV)	R_{NEEC} (s^{-1})	R_{NEIES} (s^{-1})	Dominated by	R_{iso} (s^{-1})	P
$0 \rightarrow 1$	130	0.0001	2.09×10^{-1}	2.64×10^{-1}	NEEC and NEIES	4.73×10^{-1}	1.00
$0 \rightarrow 2 \rightarrow 1$	130	2.519733	1.31	2.84×10^{-1}	NEEC and NEIES	1.59	3.37
$0 \rightarrow 3 \Rightarrow 1$	130	15.764703	0.00	2.67×10^{-1}	NEIES	2.67×10^{-1}	0.56
$0 \rightarrow 4 \Rightarrow 1$	130	41.049	4.31×10^{-3}	2.69×10^{-1}	NEIES	2.73×10^{-1}	0.58
$0 \rightarrow 5 \Rightarrow 1$	130	66.35895	4.20	2.68×10^{-1}	NEEC and NEIES	4.47	9.45
$0 \rightarrow 6 \Rightarrow 1$	130	94.6615	1.35×10^1	2.67×10^{-1}	NEEC	1.38×10^1	29.18

[1] L. A. Kroger and C. W. Reich, [Nucl. Phys. A 259, 29 \(1976\)](#).

[2] C. W. Reich and R. G. Helmer, [Phys. Rev. Lett. 64, 271 \(1990\)](#).

[3] E. V. Tkalya, V. O. Varlamov, V. V. Lomonosov, and S. A. Nikulin, [Phys. Scr. 53, 296 \(1996\)](#).

[4] E. Peik and C. Tamm, [Europhys. Lett. 61, 181 \(2003\)](#).

[5] L. von der Wense and B. Seiferle, [Eur. Phys. J. A 56, 277 \(2020\)](#).

[6] P. G. Thirolf, S. Kraemer, D. Moritz, and K. Scharl, [Eur. Phys. J. Spec. Top. 233, 1113 \(2024\)](#).

[7] S. Kraemer and P. V. Duppen, [Nucl. Phys. News 35, 19 \(2025\)](#).

[8] E. V. Tkalya, [Phys. Rev. Lett. 106, 162501 \(2011\)](#).

[9] E. Peik, T. Schumm, M. S. Safronova, A. Pálffy, J. Weitenberg, and P. G. Thirolf, [Quantum Sci. Technol. 6, 034002 \(2021\)](#).

[10] K. Beeks, G. A. Kazakov, F. Schaden, I. Morawetz, L. T. D. Col, T. Riebner, M. Bartokos, T. Sikorsky, T. Schumm, C. Zhang, T. Ooi, J. S. Higgins, J. F. Doyle, J. Ye, and M. S. Safronova, [Nat. Commun. 16, 9147 \(2025\)](#).

[11] E. Fuchs, F. Kirk, E. Madge, C. Paranjape, E. Peik, G. Perez, W. Ratzinger, and J. Tiedau, [Phys. Rev. X 15, 021055 \(2025\)](#).

[12] C. Zhang, T. Ooi, J. S. Higgins, J. F. Doyle, L. von der Wense, K. Beeks, A. Leitner, G. A. Kazakov, P. Li, P. G. Thirolf, *et al.*, [Nature 633, 63 \(2024\)](#).

[13] J. Tiedau, M. V. Okhapkin, K. Zhang, J. Thielking, G. Zitzer, E. Peik, F. Schaden, T. Pronebner, I. Morawetz, L. T. D. Col, F. Schneider, A. Leitner, M. Pressler, G. A. Kazakov, K. Beeks, T. Sikorsky, and T. Schumm, [Phys. Rev. Lett. 132, 182501 \(2024\)](#).

[14] R. Elwell, C. Schneider, J. Jeet, J. E. S. Terhune, H. W. T. Morgan, A. N. Alexandrova, H. B. T. Tan, A. Derevianko, and E. R. Hudson, [Phys. Rev. Lett. 133, 013201 \(2024\)](#).

[15] S. Kraemer, J. Moens, M. Athanasakis-Kaklamanakis, *et al.*, [Nature 617, 706 \(2023\)](#).

[16] T. Hiraki, K. Okai, M. Bartokos, *et al.*, [Nature Communications 15, 5536 \(2024\)](#).

[17] S. V. Pineda, P. Chhetri, S. Bara, *et al.*, [Phys. Rev. Res. 7, 013052 \(2025\)](#).

[18] H. W. T. Morgan, H. B. Tran Tan, R. Elwell, A. N. Alexandrova, E. R. Hudson, and A. Derevianko, [Phys. Rev. Lett. 134, 253801 \(2025\)](#).

[19] R. Masuda, T. Naito, M. Kaneko, H. Kazama, S. Hashiba, K. Misawa, and Y. Kasamatsu, [Phys. Rev. Res. 7, 043217 \(2025\)](#).

[20] C. Zhang, L. von der Wense, J. F. Doyle, J. S. Higgins, T. Ooi, H. U. Friebel, J. Ye, R. Elwell, J. E. S. Terhune, H.-W. T. Morgan, *et al.*, [Nature 636, 603 \(2024\)](#).

[21] T. Hiraki, K. Okai, M. Bartokos, K. Beeks, H. Fujimoto, Y. Fukunaga, H. Haba, Y. Kasamatsu, S. Kitao, A. Leitner, T. Masuda, M. Guan, N. Nagasawa, R. Ogake, M. Pimon, M. Pressler, N. Sasao, F. Schaden, T. Schumm, M. Seto, Y. Shigekawa, K. Shimizu, T. Sikorsky, K. Tamasaku, S. Taktori, T. Watanabe, A. Yamaguchi, Y. Yoda, A. Yoshimi, and K. Yoshimura, [Nat. Commun. 15, 5536 \(2024\)](#).

[22] R. Elwell, J. E. S. Terhune, C. Schneider, H. W. T. Morgan, H. B. T. Tan, U. C. Perera, D. A. Rehn, M. C. Alfonso, L. von der Wense, B. Seiferle, K. Scharl, P. G. Thirolf, A. Derevianko, and E. R. Hudson, [Nature 648, 300 \(2025\)](#).

[23] A. Yamaguchi, Y. Shigekawa, H. Haba, H. Kikunaga, K. Shirasaki, M. Wada, and H. Katori, [Nature 629, 62 \(2024\)](#).

[24] G. Zitzer, J. Tiedau, M. V. Okhapkin, K. Zhang, C. Mokry, J. Runke, C. E. Düllmann, and E. Peik, [Phys. Rev. A 109, 033116 \(2024\)](#).

[25] G. Zitzer, J. Tiedau, C. E. Düllmann, M. V. Okhapkin, and E. Peik, [Phys. Rev. A 111, L050802 \(2025\)](#).

[26] J. Stricker, J. Velten, V. Andriushkov, L. M. Arndt, D. Budker, K. Gaul, D. Renisch, F. Schmidt-Kaler, A. Trimeche, L. von der Wense, and C. E. Düllmann (TACTICA Collaboration), [Phys. Rev. A 112, 012821 \(2025\)](#).

[27] D. Moritz, K. Scharl, M. Wiesinger, G. Holthoff, T. Teschler, M. I. Hussain, J. R. C. López-Urrutia, T. Dickel, S. Ding, C. E. Düllmann, E. R. Hudson, S. Kraemer, L. Löbell, C. Mokry, J. Runke, B. Seiferle, L. von der Wense, F. Zacherl, and P. G. Thirolf, [Eur. Phys. J. D 79, 127 \(2025\)](#).

[28] L. von der Wense, B. Seiferle, M. Laatiaoui, J. B. Neumayr, H.-J. Maier, H.-F. Wirth, C. Mokry, J. Runke, K. Eberhardt, and C. E. Düllmann, [Nature 533, 47 \(2016\)](#).

[29] B. Seiferle, L. von der Wense, and P. G. Thirolf, [Phys. Rev. Lett. 118, 042501 \(2017\)](#).

[30] J. Thielking, M. V. Okhapkin, P. Głowacki, D. M. Meier, L. von der Wense, B. Seiferle, C. E. Düllmann, P. G. Thirolf, and E. Peik, [Nature 556, 321 \(2018\)](#).

[31] B. Seiferle, L. von der Wense, P. V. Bilous, I. Amersdorffer, C. Lemell, F. Libisch, S. Stellmer, T. Schumm, C. E. Düllmann, A. Pálffy, *et al.*, [Nature 573, 243 \(2019\)](#).

[32] A. Yamaguchi, H. Muramatsu, T. Hayashi, N. Yuasa, K. Nakamura, M. Takimoto, H. Haba, K. Konashi, M. Watanabe, H. Kikunaga, K. Maehata, N. Y. Yamasaki, and K. Mitsuda, [Phys. Rev. Lett. 123, 222501 \(2019\)](#).

[33] S. Kraemer, J. Moens, M. Athanasakis-Kaklamanakis, S. Bara, K. Beeks, P. Chhetri, K. Chrysalidis, A. Claessens, T. E. Cocolios, and J. G. M. Correia, [Nature 617, 706 \(2023\)](#).

[34] M. Verlinde, S. Kraemer, J. Moens, K. Chrysalidis, J. G. Correia, S. Cottenier, H. De Witte, D. V. Fedorov, V. N. Fedosseev, R. Ferrer, L. M. Fraile, S. Geldhof, C. A. Granados, M. Laatiaoui, T. A. L. Lima, P.-C. Lin, V. Manea, B. A.

Marsh, I. Moore, L. M. C. Pereira, S. Raeder, P. Van den Bergh, P. Van Duppen, A. Vantomme, E. Verstraelen, U. Wahl, and S. G. Wilkins, *Phys. Rev. C* **100**, 024315 (2019).

[35] J. Thielking, K. Zhang, J. Tiedau, J. Zander, G. Zitzer, M. V. Okhapidze, and E. Peik, *New J. Phys.* **25**, 083026 (2023).

[36] Q. Xiao, G. Penyazkov, R. Yu, B. Huang, J. Li, J. Shi, Y. Yu, Y. Mo, and S. Ding, arXiv:2406.16841 [10.48550/arXiv.2406.16841](https://arxiv.org/abs/2406.16841) (2024).

[37] V. Lal, M. V. Okhapidze, J. Tiedau, N. Irwin, V. Petrov, and E. Peik, *Optica* **12**, 1971 (2025).

[38] T. Masuda, A. Yoshimi, A. Fujieda, H. Fujimoto, H. Haba, H. Hara, T. Hiraki, H. Kaino, Y. Kasamatsu, S. Kitao, *et al.*, *Nature* **573**, 238 (2019).

[39] G. M. Temmer and N. P. Heydenburg, *Phys. Rev.* **104**, 989 (1956).

[40] E. V. Tkalya, *Phys. Rev. Lett.* **124**, 242501 (2020).

[41] H. Zhang and X. Wang, *Front. Phys.* **11**, 1166566 (2023).

[42] H. Zhang, W. Wang, and X. Wang, *Phys. Rev. C* **106**, 044604 (2022).

[43] Y.-Y. Xu, J.-H. Cheng, Y.-T. Zou, Q. Xiao, and T.-P. Yu, *Phys. Rev. C* **110**, 064621 (2024).

[44] Z. H. A. Pálffy, W. Scheid, *Phys. Rev. A* **73**, 012715 (2006).

[45] C. H. K. A. Pálffy, J. Evers, *Phys. Rev. Lett.* **99**, 172502 (2007).

[46] C. Chiara, J. Carroll, M. Carpenter, J. Greene, D. Hartley, R. Janssens, G. Lane, J. Marsh, D. Matters, M. Polasik, *et al.*, *Nature* **554**, 216 (2018).

[47] S. Gargiulo, I. Madan, and F. Carbone, *Phys. Rev. Lett.* **128**, 212502 (2022).

[48] Y. Wang, Z. Ma, Y. Yang, C. Fu, W. He, and Y. Ma, *Front. Phys.* **11**, 1203401 (2023).

[49] J. Zhao, A. Pálffy, C. H. Keitel, and Y. Wu, *Phys. Rev. C* **110**, 014330 (2024).

[50] Y. Yang, Y. Wang, Z. Ma, C. Fu, W. He, and Y. Ma, *Front. Phys.* **12**, 1410076 (2024).

[51] Y. Yang, H.-X. Zhang, Y.-B. Wu, S. Guo, X. Wang, C.-B. Fu, Y. Sun, and Y.-G. Ma, *Nucl. Sci. Tech.* **36**, 146 (2025).

[52] Y.-Y. Xu, Q. Xiao, J.-H. Cheng, W.-Y. Zhang, and T.-P. Yu, arXiv preprint arXiv:2510.08212 [10.48550/arXiv.2510.08212](https://arxiv.org/abs/2510.08212) (2025).

[53] W. Wang, J. Zhou, B. Liu, and X. Wang, *Phys. Rev. Lett.* **127**, 052501 (2021).

[54] K. Koziol and J. Rzadkiewicz, *Phys. Rev. C* **111**, 064302 (2025).

[55] Y. Wu, C. H. Keitel, and A. Pálffy, *Phys. Rev. Lett.* **122**, 212501 (2019).

[56] S. Guo, B. Ding, X. H. Zhou, Y. B. Wu, J. G. Wang, S. W. Xu, Y. D. Fang, C. M. Petrache, E. A. Lawrie, Y. H. Qiang, Y. Y. Yang, H. J. Ong, J. B. Ma, J. L. Chen, F. Fang, Y. H. Yu, B. F. Lv, F. F. Zeng, Q. B. Zeng, H. Huang, Z. H. Jia, C. X. Jia, W. Liang, Y. Li, N. W. Huang, L. J. Liu, Y. Zheng, W. Q. Zhang, A. Rohilla, Z. Bai, S. L. Jin, K. Wang, F. F. Duan, G. Yang, J. H. Li, J. H. Xu, G. S. Li, M. L. Liu, Z. Liu, Z. G. Gan, M. Wang, and Y. H. Zhang, *Phys. Rev. Lett.* **128**, 242502 (2022).

[57] J. Rzadkiewicz, M. Polasik, K. Słabkowska, L. Syrocki, J. J. Carroll, and C. J. Chiara, *Phys. Rev. Lett.* **127**, 042501 (2021).

[58] J. Rzadkiewicz, K. Słabkowska, M. Polasik, L. Syrocki, J. J. Carroll, and C. J. Chiara, *Phys. Rev. C* **108**, L031302 (2023).

[59] M. G. Kozlov, M. S. Safranova, J. R. Crespo López-Urrutia, and P. O. Schmidt, *Rev. Mod. Phys.* **90**, 045005 (2018).

[60] B. Tu, N. Xue, J. Liu, Q. Guo, Y. Wu, Z. Liu, A. Pálffy, Y. Yang, K. Yao, B. Wei, Y. Zou, X. Kong, and Y.-G. Ma, *Phys. Rev. C* **112**, 054307 (2025).

[61] National Nuclear Data Center, Nudat 3.0 nuclear structure database, <https://www.nndc.bnl.gov/nudat3/>, accessed 2025.

[62] F. Bosch, Y. A. Litvinov, and T. Stöhlker, *Prog. Part. Nucl. Phys.* **73**, 84 (2013).

[63] X. Ma, W. Wen, Z. Huang, H. Wang, Y. Yuan, M. Wang, Z. Sun, L. Mao, J. Yang, H. Xu, *et al.*, *Phys. Scr.* **2015**, 014012 (2015).

[64] J. Jin, H. Bekker, T. Kirschbaum, Y. A. Litvinov, A. Pálffy, J. Sommerfeldt, A. Surzhykov, P. G. Thirolf, and D. Budker, *Phys. Rev. Res.* **5**, 023134 (2023).

[65] Y. Fu, K. Yao, B. Wei, D. Lu, R. Hutton, and Y. Zou, *J. Instrum.* **5** (08), C08011.

[66] L. Prokhorov, A. A. Smith, M. Xu, K. Georgiou, V. Guarnera, L. P. K. Sajith, E. A. Dijck, C. Warnecke, M. Wehrheim, A. Wilzewski, *et al.*, arXiv **2512.12266**, [10.48550/arXiv.2512.12266](https://arxiv.org/abs/2512.12266) (2025).

[67] J. Qi, H. Zhang, and X. Wang, *Phys. Rev. Lett.* **130**, 112501 (2023).

[68] Z.-R. Chen, L.-J. Wang, and Y. Wu, *Phys. Lett. B* **869**, 139858 (2025).

[69] F. Salvat and J. M. Fernández-Varea, *Comput. Phys. Commun.* **240**, 165 (2019).

[70] J. C. Slater, *Phys. Rev.* **81**, 385 (1951).

[71] D. Liberman, D. Cromer, and J. Waber, *Comput. Phys. Commun.* **2**, 107 (1971).

[72] K. Lee, A. Stratman, C. Casarella, A. Aprahamian, and S. Lesher, *Comput. Phys. Commun.* **306**, 109383 (2025).

[73] Q. Xiao, Y.-Y. Xu, J.-H. Cheng, L.-Q. Zhang, W.-Y. Zhang, Y.-S. Huang, and T.-P. Yu, *Phys. Rev. C* **112**, 064313 (2025).

[74] J. Ringuette and Z. Hockenberry, ebitsim: Ebit charge breeding simulation, <https://github.com/TITANCollaboration/ebitsim> (2025), accessed: 2026-01-02.

[75] B. Wallis, *Optimising the experimental approach to Nuclear Excitation by Electron Capture*, Ph.D. thesis, University of York (2021).